

Depth-resolved magnetic and structural analysis of relaxing epitaxial Sr₂CrReO₆J. M. Lucy,¹ A. J. Hauser,² Y. Liu,³ H. Zhou,⁴ Y. Choi,⁴ D. Haskel,⁴ S. G. E. te Velthuis,³ and F. Y. Yang^{1,*}¹*Department of Physics, The Ohio State University, 191 West Woodruff Avenue, Columbus, Ohio 43210, USA*²*California Nanosystems Institute, Elings Hall, University of California, Santa Barbara, California 93106, USA*³*Materials Science Division, Argonne National Laboratory, 9700 South Cass Avenue, Argonne, Illinois 60439, USA*⁴*Advanced Photon Source, Argonne National Laboratory, 9700 South Cass Avenue, Argonne, Illinois 60439, USA*

(Received 5 January 2015; revised manuscript received 12 February 2015; published 16 March 2015)

Structural relaxation in a Sr₂CrReO₆ epitaxial film, which exhibits strong spin-orbit coupling, leads to depth-dependent magnetism. We combine two depth-resolved synchrotron x-ray techniques—two-dimensional reciprocal space mapping and x-ray magnetic circular dichroism—to quantitatively determine this effect. An 800-nm-thick film of Sr₂CrReO₆, grown with tensile epitaxial strain on SrCr_{0.5}Nb_{0.5}O₃(225 nm)/(LaAlO₃)_{0.3}(Sr₂AlTaO₆)_{0.7}, relaxes away from the Sr₂CrReO₆/SrCr_{0.5}Nb_{0.5}O₃ interface to its bulk lattice parameters, with much of the film being fully relaxed. Grazing incidence x-ray diffraction of the film elucidates the in-plane strain relaxation near the film-substrate interface, while depth-resolved x-ray magnetic circular dichroism at the Re *L* edge reveals the magnetic contributions of the Re site. The smooth relaxation of the film near the interface correlates with changes in the magnetic anisotropy. This provides a systematic and powerful way to probe the depth-varying structural and magnetic properties of a complex oxide with synchrotron-source x-ray techniques.

DOI: [10.1103/PhysRevB.91.094413](https://doi.org/10.1103/PhysRevB.91.094413)

PACS number(s): 75.30.Gw, 76.60.Es, 68.55.-a, 75.25.-j

I. INTRODUCTION

Epitaxial strain is an important mechanism in thin films that can simultaneously affect structural, electronic, optical, thermal, and magnetic properties. For tuning of electronic properties, epitaxial strain is often present in heteroepitaxial devices such as optoelectronic and band-gap-engineered structures [1]. Magnetic properties can be readily tuned by structural distortions (via strain), particularly in materials exhibiting strong magnetocrystalline anisotropy (MCA). MCA is a product of spin-orbit coupling, wherein the electronic spin moments couple to the orbital moments, and thus the lattice. Even small epitaxial strains (less than 1%) can have drastic effects on magnetic properties in materials exhibiting large MCA [2–6].

For small coherent strains in thin films, it is expected that the strain will obey elasticity theory without severely perturbing the crystal growth. In this regime, of approximately 1% strain or less $\{ \text{strain } f = [a_0(\text{substrate}) - a_0(\text{film})]/[a_0(\text{film})] \}$, films can be grown up to a critical thickness before strain relaxation takes place. Below the critical thickness, the elastically strained structure remains thermodynamically stable, while above it the lattice can relax [7] via mechanisms such as the onset of misfit dislocations or, particularly in oxides, strain accommodation by oxygen vacancies. In thin films ranging from hundreds of nanometers to several micrometers in thickness, strain relaxation is important and, in materials exhibiting large MCA, can lead to correlated and depth-dependent structural and magnetic behavior.

Materials in the class of double perovskites have been shown to possess a variety of interesting properties (e.g., room-temperature magnetoresistance in Sr₂FeMoO₆ [8]). These materials, such as Sr₂CrReO₆ (the focus of this study), are strongly correlated electronic systems that provide

opportunities for interesting experimental and theoretical studies [9–11]. We have previously explored the spin and orbital magnetic moment contributions by Cr, Re, and O in Sr₂CrReO₆ (SCRO) films using x-ray magnetic circular dichroism [2,12,13]. We have also demonstrated extraordinarily large MCA in SCRO films, which is tunable via epitaxial strain [3]. Here, we report depth-resolved studies of the magnetic and structural properties of an 800 nm SCRO epitaxial film grown on a 225 nm buffer layer of SrCr_{0.5}Nb_{0.5}O₃ (SCNO) on a (LaAlO₃)_{0.3}(Sr₂AlTaO₆)_{0.7} (LSAT) substrate. The buffer layer imposes approximately 1% tensile strain on the SCRO film and the film relaxes away from the buffer layer interface. We combine two synchrotron-source x-ray techniques, namely depth-resolved two-dimensional reciprocal space mapping via grazing incidence x-ray diffraction (GIXD) and depth-resolved x-ray magnetic circular dichroism (XMCD), to show correlation between structural distortions and magnetic behavior in the relaxing 800 nm SCRO film.

II. FILM GROWTH AND PROFILE DETAILS

The SCRO and SCNO layers were deposited using an off-axis ultrahigh-vacuum magnetron sputtering technique we have developed in recent years [3,4,14–20]. The nonmagnetic and insulating SCNO buffer layer was deposited to a thickness of 225 nm on an LSAT substrate. The large mismatch between the buffer layer and substrate lattice constants (just over 2% mismatch) causes the buffer layer to quickly relax away from the substrate interface to nearly its bulk lattice constants. An 800 nm SCRO film was then deposited directly onto the buffer layer. The result, as previously mentioned, is a relaxing 800 nm SCRO film with imposed tensile strain at the buffer layer interface.

We use a Bruker D8 Discover high-resolution triple-axis x-ray diffractometer to characterize the overall structural profile of the heterostructure. Figure 1 shows the $\theta/2\theta$ x-ray diffraction (XRD) scan around the LSAT (002), SCNO (002),

*fyyang@physics.osu.edu

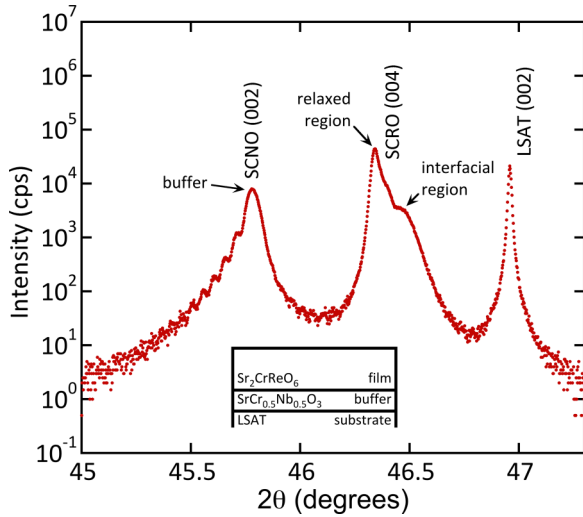


FIG. 1. (Color online) XRD scan around the $\text{Sr}_2\text{CrReO}_6$ (004) peak for the 800 nm $\text{Sr}_2\text{CrReO}_6$ film grown on a 225 nm buffer layer of $\text{SrCr}_{0.5}\text{Nb}_{0.5}\text{O}_3$ on LSAT. The $\text{Sr}_2\text{CrReO}_6$ (004) peak exhibits two features: one corresponding to the interfacial region epitaxially strained (tensile in-plane strain) to the buffer layer, and one representing the relaxed region of the film. The inset depicts the heterostructure growth profile.

and SCRO (004) peaks, which allows measurement of the out-of-plane lattice constants. An XRD scan (not shown) was performed at a tilt angle $\Psi = 45^\circ$ for diffraction of the SCRO (022) and SCNO (011) planes in order to characterize the in-plane lattice constants. The inset in Fig. 1 depicts the heterostructure growth profile.

First, we observe both the SCRO (004) and SCNO (002) peaks, which are clearly distinguishable from the LSAT substrate peak due to the differences in out-of-plane lattice constants.

The SCNO (002) peak shows asymmetry, which is evidence of its relaxing structure away from the LSAT interface, and it exhibits Laue oscillations, demonstrating its smoothness and uniformity. Meanwhile, Laue oscillations from the 800 nm SCRO film cannot be resolved due to its large thickness. The SCRO (004) peak reveals two characteristic features (labeled in Fig. 1). One corresponds to the SCRO-SCNO interfacial strained region and the other corresponds to the relaxed region of the 800 nm SCRO film. The choice of which feature represents the strained interfacial region (shown at higher 2θ in Fig. 1) is determined by previous experiments with thinner, fully strained SCRO films on SCNO [3]. In addition, for tensile strain such as that at the buffer layer interface, the out-of-plane axis will contract, resulting in a diffraction peak at a larger angle. The feature corresponding to the relaxed region of the film is much stronger than that corresponding to the strained interfacial region, and a smooth shoulder connects the two. This suggests that much of the film is fully relaxed while strain relaxation occurs near the substrate interface. The ratio of the two characteristic SCRO peak intensities suggests that approximately 100 nm of the SCRO film is strained or relaxing, while the remaining thickness of the film is fully relaxed.

XRD results give the average lattice constants of the SCNO buffer layer and the SCRO film. The SCNO buffer layer has

lattice constants (in-plane) $2a_p = 7.892 \text{ \AA}$ and (out-of-plane) $2c = 7.960 \text{ \AA}$. The SCRO interfacial strained region gives average lattice constants $a_p = 7.872 \text{ \AA}$ and $c = 7.810 \text{ \AA}$ ($c/a_p = 0.992$), and the SCRO relaxed region gives average lattice constants $a_p = 7.812 \text{ \AA}$ and $c = 7.830 \text{ \AA}$ ($c/a_p = 1.002$). The subscript p denotes the pseudocubic double perovskite unit cell. The in-plane lattice parameters reveal that the SCNO buffer layer imposes approximately 1.1% tensile strain on the SCRO film at the buffer layer interface.

III. MAGNETIC PROPERTIES

In our previous work, we used XMCD to quantify the spin and orbital moment contributions of the Cr and Re sites in SCRO films for three instances of epitaxial strain: (approximately) 0.8% compressive strain imposed by an LSAT substrate, 0.15% tensile/nominally relaxed strain imposed by a SrTiO_3 (STO) substrate, and 1.1% tensile strain imposed by an SCNO buffer layer on LSAT [2]. Previous experiments also demonstrated the strain-tunable and strong MCA in SCRO films, which is driven primarily by the Re sites. These experiments show that the magnetic easy axis flips from in plane to out of plane, depending on the epitaxial strain imposed by the substrate. The easy axis remained in plane for SCRO films grown on compressive (LSAT substrate) or relaxed (STO substrate) strains and flipped to out of plane for SCRO films grown on tensile (SCNO buffer layer on LSAT) strain. This flipping of the easy axis corresponds to a change in sign of the MCA [3]. Interpolation suggested MCA should change sign at a tensile strain of about 0.30%, in agreement with the value predicted by previous density-functional theory (DFT) generalized gradient approximation (GGA) calculations [21].

For the present work, we expect that within the 800 nm SCRO film, near the interface, there is a smooth relaxation from large tensile strain to nominally relaxed strain (crossing the 0.3% threshold for flipping of the MCA), likely mediated by the presence of oxygen vacancies. Since Re has been shown to drive the switching of MCA [3], we focus here on XMCD of the Re L edge. Figure 2 shows the x-ray absorption (XAS) and XMCD spectra for the Re L_2 edge for an x-ray penetration depth of 1384 nm at a temperature $T = 200 \text{ K}$. The x-ray penetration depth, δ_p , is defined as the depth in the film at which the x-ray intensity drops off to $1/e$ its incident value and is controlled via the grazing incidence angle of the x rays relative to the film surface, such as in Ref. [22]. The maximum grazing angle used in the experiments is 8.65° , so that shape anisotropy effects can be neglected.

As can be seen in Fig. 2, there is a readily apparent XMCD signal at the Re L_2 edge that allows observation of magnetic behavior of the Re sites. To better probe the smooth transition of magnetization at the Re sites as the SCRO film relaxes away from the buffer layer interface, we measure magnetic hystereses at various x-ray penetration depths using XMCD. The hystereses are measured by fixing the x-ray energy to the peak position of the Re L_2 edge ($E = 11.965 \text{ keV}$) and sweeping the in-plane magnetic field between $+3.5 \text{ T}$ and -3.5 T . The XAS and XMCD data were recorded at each field value. To account for variance in the incident x-ray intensity and changes in the Re L edge white line intensity (which may

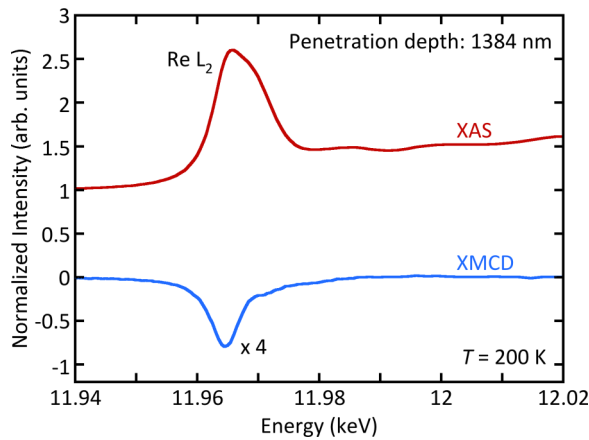


FIG. 2. (Color online) XAS and XMCD spectra for the Re L_2 edge at an x-ray penetration depth of 1384 nm from the SCRO film surface. The spectra are recorded at a temperature $T = 200$ K. The penetration depth, δ_p , defined as the depth in the film at which the x-ray intensity drops to $1/e$ its incident value, is controlled via the grazing incidence angle.

be depth-dependent due to strain), the resultant hystereses are plotted as the ratio of the XMCD to XAS signals.

Figure 3(a) shows the Re L_2 XMCD/XAS hysteresis loops for nine different x-ray penetration depths: 3, 87, 158, 228, 299, 384, 553, 922, and 1384 nm from the film surface. Across the Re L_2 absorption edge, the absorption length and the critical angle for total external reflection vary significantly due to changes in the absorption cross section of Re. We calculate the absorption length and critical angle for total external reflection using the Re L_2 XAS data from the sample of interest. The results are shown in Fig. 3(b). Using these values, we estimate the penetration depth for each incident angle used for the hysteresis loops shown in Fig. 3(a). The penetration depth calculations include refraction corrections for the incident angles. The attenuation of the emitted Re L_β fluorescence within the film was neglected (at most a 5% change) since the absorption length of the Re L_β (19,100 nm) within the SCRO film is much longer than the total film thickness (800 nm).

It should be noted that due to x-ray attenuation, data measured in the grazing incidence geometry are convoluted. The detected signal is primarily determined by the attenuation of incident x rays since the attenuation of the emitted Re L_β fluorescence within the film is small. To aid the reader in visualizing the effects of convolution, we show in Fig. 4 the relative contributions of regions in the film as functions of the depth from the surface. It is readily seen that as the grazing angle is increased, the effective sampling of regions near the film–substrate interface increases. For example, at a penetration depth of 87 nm (magenta circles) there is almost no contribution from regions beyond 350 nm from the film surface. This fact remains for structural measurements that will be discussed in the next section.

The first penetration depth of 3 nm is measured using an incident angle below the critical angle, and so the data are sensitive to only the top few nanometers of the film. Near the surface of the film, the SCRO structure is expected to be fully relaxed with a structure similar to that of epitaxial SCRO/STO,

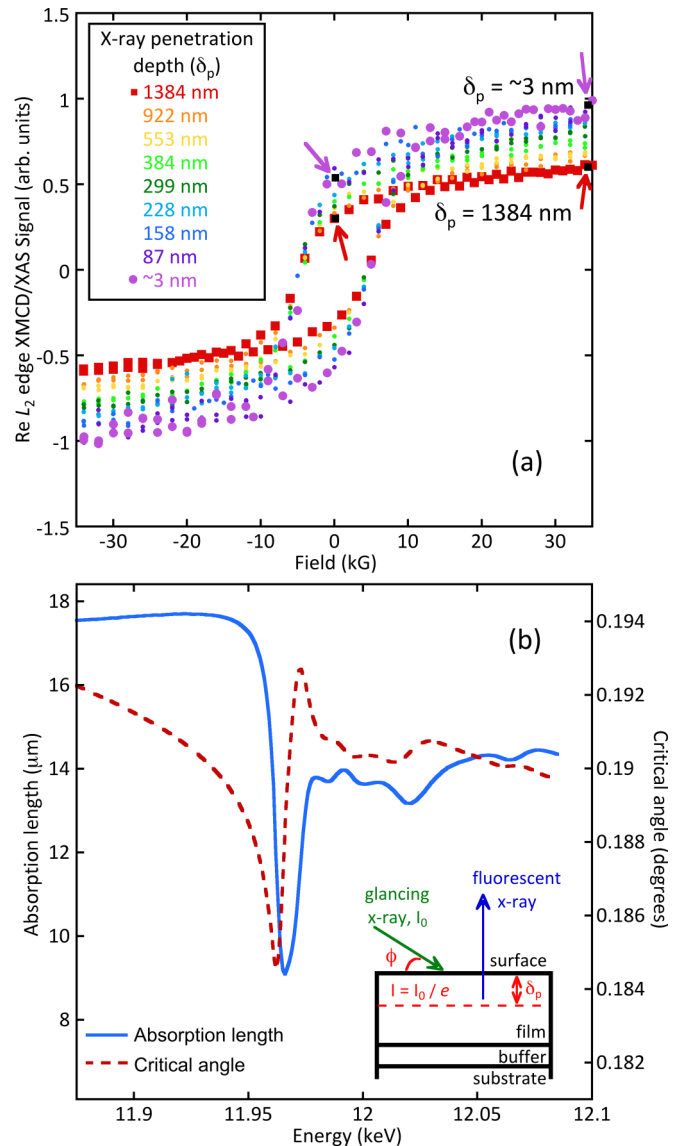


FIG. 3. (Color online) (a) Magnetic hysteresis loops measured in the grazing incidence x-ray geometry shown [inset in panel (b)] for various x-ray penetration depths. The x-ray intensity at the penetration depth, δ_p , is $I = I_0/e$, where I_0 is the incident intensity at the film surface. External magnetic fields are applied along the incident x-ray direction, essentially in the film plane, at grazing angles. The loops are scaled for separation and visual clarity. (b) Absorption length (μm) and critical angle (deg) of the SCRO film as functions of x-ray energy near the Re L absorption edge.

as in Ref. [2]. Thus, near the surface the easy magnetic axis should be in the plane of the film. Near the SCNO buffer layer interface, however, it is expected that the tensile strain should flip the magnetic easy axis to out of plane. The smooth transition between these two regimes is observable in Fig. 3(a). We intentionally plot the various penetration depths following the colors of the visible spectrum to guide the eye. At a penetration depth of 3 nm (magenta circles), one can see that the hysteresis loop is more square than the loop shown for a penetration depth of 1384 nm (red squares). Since the hysteresis loops shown do not represent measurable magnetic moments (integrated edge intensities are needed for that), one

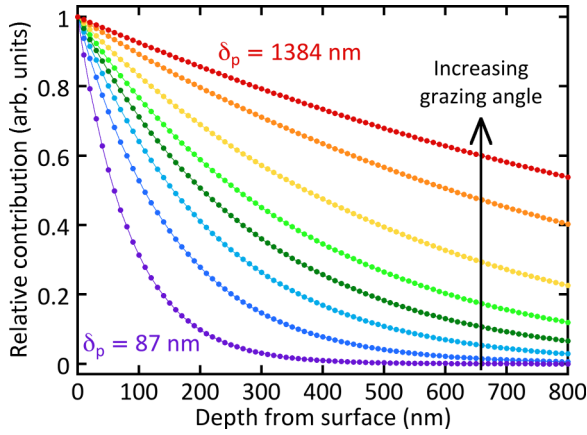


FIG. 4. (Color online) Relative contributions to the detected signal of depths within the SCRO film (from the surface) plotted for various grazing incident angles [following the same color scheme as Fig. 3(a)]. As the grazing angle is increased, so is the relative contribution of regions near the film-substrate interface.

should not compare the magnitudes of the loops. However, the loops are self-consistent and their shapes (such as squareness) can be compared.

To quantify the squareness of the hysteresis loops shown in Fig. 3(a), we compare the remanent and high-field (3.5 T) magnetizations and plot the ratio as a function of x-ray penetration depth. Remanent and high-field magnetizations were obtained from the hysteresis loops via smooth fitting of the data near these field regimes. The magenta and red arrows in Fig. 3(a) denote points used for the squareness calculations of the two extreme penetration depths (3 and 1384 nm), but the actual values of these points are dependent on normalization (whereas their ratio is not), and we do not provide the values here. The results of the squareness calculations are shown in Fig. 5(a), with error bars denoting systematic error due to fitting of the hysteresis loops.

The ratio of the remanent to high-field magnetizations can be thought of as a measure of the easiness of the magnetic axis being probed (here, we apply magnetic fields in the plane of the film). Thus, in Fig. 5(a), ratios closer to 0 represent a hard axis and ratios closer to 1 represent an easy axis in the film plane. As expected, near the surface of the film the squareness is closer to 1, while at larger penetration depths the squareness moves toward 0. We expect the squareness to approach a terminal value as the x-ray grazing angles reach large values since the 800 nm SCRO film becomes more uniformly sampled (see Fig. 4). The in-plane field of 3.5 T is strong enough to nearly fully saturate regions of the film with in-plane easy axes, but regions with out-of-plane easy axes will give squareness values farther away from 0 as they are not nearly fully saturated [2,3]. This effect, along with convolution due to x-ray attenuation in the film, leads to a narrow window of squareness values achieved from the data. However, the variation is systematic and readily observable.

IV. STRUCTURAL AND MAGNETIC CORRELATION

Figure 5 also shows, in panel (b), structural information as a function of x-ray penetration depth. We use grazing incidence

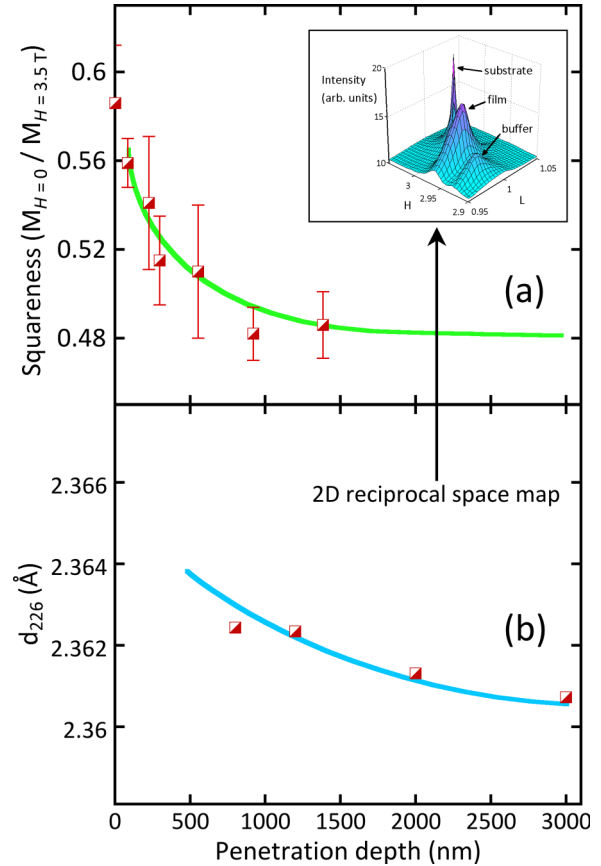


FIG. 5. (Color online) (a) Squareness of the hysteresis loops of Fig. 3, where squareness approaching 1 corresponds to an in-plane magnetic easy axis. (b) d spacings of the SCRO (226) planes obtained using two-dimensional reciprocal space mapping in the grazing incidence x-ray diffraction geometry for various x-ray penetration depths. An inset is provided in panel (a) to show an example of raw RSM data. The solid curves are guides to the eye.

x-ray diffraction (GIXD) along with two-dimensional reciprocal space mapping (RSM) to determine the spacing of the (226) planes in the SCRO film as a function of x-ray penetration depth. We perform HKL mesh scans around the (113) Bragg reflection for the LSAT substrate, fixing $K = 1$, while using a GIXD geometry to control the x-ray penetration depth. The (226) and (113) Bragg reflections for the SCRO and SCNO layers, respectively, are also seen in these scans. An example of the raw RSM data is shown in the inset in Fig. 5(a). Fits of the HKL positions for the SCRO (226) peaks allow the spacings of the planes to be determined for various x-ray penetration depths. It should be noted that the structural data are convoluted by the spatial exponential decay of the x rays. Deconvolution requires a thorough knowledge of the complete strain profile, and such data are not presented here.

Fitting of the two-dimensional reciprocal space map data was performed utilizing the built-in MATLAB curve-fitting tool with custom fit functions. The two dominant peaks in each spectrum, namely the substrate and film peaks, were each fit with a two-dimensional rotated elliptical Gaussian. The overall fits for the maps resulted in average R^2 (goodness of fit) values >0.998 . Fitting of the peaks provided the HKL positions (with

fixed $K = 1$), from which we calculated the reflection angle, 2θ , according to Bragg's law. It is important to note that all HKL values reported by the diffractometer are in reference to the orientation matrix of the LSAT substrate, so that

$$n\lambda = 2 \frac{a_{\text{LSAT}}}{(H^2 + K^2 + L^2)^{1/2}} \sin(\theta). \quad (1)$$

In other words, the reflection angle of the detector is determined by the HKL values of the LSAT substrate.

To determine d spacings from the calculated detector angles, refraction corrections must be made. Refraction corrections are important for grazing incidence x-ray geometries, particularly when measurements are sensitive to the scattering vector (such as in Bragg diffraction). We follow the model of Toney *et al.* [23] to find the angle correction, $2\Delta\theta$,

$$2\Delta\theta \approx \phi - \frac{1}{\sqrt{2}} \{ [(\phi^2 - \phi_c^2)^2 + 4\beta^2]^{1/2} - \phi_c^2 + \phi^2 \}^{1/2}, \quad (2)$$

where ϕ is the grazing incidence angle, ϕ_c is the critical angle of either the film or substrate (depending on which peak is being analyzed), and β is the imaginary part of the index of refraction given by $\lambda\mu/4\pi$ (μ is the linear absorption coefficient). For SCRO (LSAT), we use $\phi_c = 0.178^\circ$ ($\phi_c = 0.176^\circ$) and $\beta = 2.31 \times 10^{-7}$ ($\beta = 1.92 \times 10^{-7}$). Determination of these factors was achieved through combined reflectivity measurements on the diffractometer and calculations according to LBL and NIST resources [24,25].

Once both the film and substrate peaks are corrected for refraction effects, we must also correct for any instrument misalignment by shifting the substrate peak to its standard position, which should not show depth dependence and should remain fixed at (HKL) = (113). The misalignment corrections applied to the substrate peaks are therefore equally applied to the film peaks for each x-ray penetration depth.

The d spacings of SCRO (226) planes given in Fig. 5(b) are largely representative of the out-of-plane lattice constant, c , since these planes make a relatively small angle ($\approx 25.2^\circ$) with the film plane. From previous experiments, it is known that the magnetic easy axis aligns with the short axis of the unit cell [2,3]. Thus, at the surface of the 800 nm SCRO film, where the short axis of the unit cell lies in-plane, the magnetic

easy axis should align in-plane. Meanwhile, near the buffer layer interface, the short axis of the unit cell lies out-of-plane, resulting in an out-of-plane magnetic easy axis. The squareness values given in Fig. 5(a) corroborate these expectations and demonstrate the correlated structural and magnetic behavior in the relaxing 800 nm SCRO film.

V. CONCLUSIONS

In conclusion, we demonstrate correlated magnetic and structural behavior in an 800 nm SCRO film, which relaxes away from the SCNO buffer layer interface, using complementary synchrotron XAS/XMCD, reciprocal space mapping, and x-ray diffraction techniques. The buffer layer imposes tensile strain on the SCRO film, resulting in an out-of-plane magnetic easy axis near the buffer layer interface. Strain relaxation near the buffer layer interface causes a smooth transition to an in-plane magnetic easy axis. XMCD data at an x-ray penetration depth of 1384 nm confirm readily measurable magnetism at the Re site. XMCD hysteresis loops over many x-ray penetration depths demonstrate the smooth transition of magnetism, which is well correlated to the structural relaxation shown using two-dimensional reciprocal space mapping in the grazing incidence x-ray diffraction geometry.

ACKNOWLEDGMENTS

This work is supported by the Center for Emergent Materials at the Ohio State University, a National Science Foundation Materials Research Science and Engineering Center (Grant No. DMR-1420451). Partial support is provided by the NanoSystems Laboratory and the Center for Electron Microscopy and Analysis at the Ohio State University. A.J.H. acknowledges support through an Elings Prize Fellowship of the California Nanosystems Institute at the University of California, Santa Barbara. Work at MSD, ANL (Y.L. and S.t.V.) was supported by the U.S. Department of Energy (DOE), Office of Science, Basic Energy Sciences, Materials Sciences and Engineering Division. This research used resources (GIXD and XMCD) of the Advanced Photon Source, a U.S. DOE Office of Science User Facility operated for the DOE Office of Science by Argonne National Laboratory under Contract No. DE-AC02-06CH11357.

-
- [1] R. A. Soref, *Proc. IEEE* **81**, 1687 (1993).
 - [2] A. J. Hauser, J. M. Lucy, M. W. Gaultois, M. R. Ball, J. R. Soliz, Y. Choi, O. D. Restrepo, W. Windl, J. W. Freeland, D. Haskel, P. M. Woodward, and F. Yang, *Phys. Rev. B* **89**, 180402(R) (2014).
 - [3] J. M. Lucy, M. R. Ball, O. D. Restrepo, A. J. Hauser, J. R. Soliz, J. W. Freeland, P. M. Woodward, W. Windl, and F. Y. Yang, *Phys. Rev. B* **90**, 180401(R) (2014).
 - [4] C. Du, R. Adur, H. Wang, A. J. Hauser, F. Yang, and P. C. Hammel, *Phys. Rev. Lett.* **110**, 147204 (2013).
 - [5] H. Wang, C. Du, P. C. Hammel, and F. Yang, *Phys. Rev. B* **89**, 134404 (2014).
 - [6] P. Lukashev, N. Horrell, and R. Sabirianov, *J. Appl. Phys.* **111**, 07A318 (2012).
 - [7] D. Dunstan, *J. Mater. Sci.: Mater. Electron.* **8**, 337 (1997).
 - [8] K.-I. Kobayashi, T. Kimura, H. Sawada, K. Terakura, and Y. Tokura, *Nature (London)* **395**, 677 (1998).
 - [9] H. Asano, N. Kozuka, A. Tsuzuki, and M. Matsui, *Appl. Phys. Lett.* **85**, 263 (2004).
 - [10] G. Vaitheeswaran, V. Kanchana, and A. Delin, *Appl. Phys. Lett.* **86**, 032513 (2005).
 - [11] G. Vaitheeswaran, V. Kanchana, M. Alouani, and A. Delin, *Europhys. Lett.* **84**, 47005 (2008).
 - [12] B. T. Thole, P. Carra, F. Sette, and G. van der Laan, *Phys. Rev. Lett.* **68**, 1943 (1992).
 - [13] C. T. Chen, Y. U. Idzerda, H.-J. Lin, N. V. Smith, G. Meigs, E. Chaban, G. H. Ho, E. Pellegrin, and F. Sette, *Phys. Rev. Lett.* **75**, 152 (1995).

- [14] A. J. Hauser, J. R. Soliz, M. Dixit, R. E. A. Williams, M. A. Susner, B. Peters, L. M. Mier, T. L. Gustafson, M. D. Sumption, H. L. Fraser, P. M. Woodward, and F. Y. Yang, *Phys. Rev. B* **85**, 161201(R) (2012).
- [15] J. Lucy, A. Hauser, H. Wang, J. Soliz, M. Dixit, R. Williams, A. Holcombe, P. Morris, H. Fraser, D. McComb, P. Woodward, and F. Yang, *Appl. Phys. Lett.* **103**, 042414 (2013).
- [16] A. Hauser, J. Lucy, H. Wang, J. Soliz, A. Holcomb, P. Morris, P. Woodward, and F. Yang, *Appl. Phys. Lett.* **102**, 032403 (2013).
- [17] B. Peters, A. Alfonsov, C. Blum, S. Hageman, P. Woodward, S. Wurmehl, B. Büchner, and F. Yang, *Appl. Phys. Lett.* **103**, 162404 (2013).
- [18] A. J. Hauser, R. E. A. Williams, R. A. Ricciardo, A. Genc, M. Dixit, J. M. Lucy, P. M. Woodward, H. L. Fraser, and F. Yang, *Phys. Rev. B* **83**, 014407 (2011).
- [19] H. L. Wang, C. H. Du, Y. Pu, R. Adur, P. C. Hammel, and F. Y. Yang, *Phys. Rev. B* **88**, 100406(R) (2013).
- [20] C. H. Du, H. L. Wang, Y. Pu, T. L. Meyer, P. M. Woodward, F. Y. Yang, and P. C. Hammel, *Phys. Rev. Lett.* **111**, 247202 (2013).
- [21] M. Komelj, *Phys. Rev. B* **82**, 012410 (2010).
- [22] D. Haskel, Y. Choi, D. Lee, J. Lang, G. Srajer, J. Jiang, and S. Bader, *J. Appl. Phys.* **93**, 6507 (2003).
- [23] M. F. Toney and S. Brennan, *Phys. Rev. B* **39**, 7963 (1989).
- [24] http://henke.lbl.gov/optical_constants/atten2.html.
- [25] <http://physics.nist.gov/PhysRefData/FFast/html/form.html>.